INORGANIC CHEMISTRY

FRONTIERS

RESEARCH ARTICLE

Check for updates

Facile assembly of a graphitic carbon nitride film at an air/water interface for photoelectrochemical NADH regeneration†

Changchao Jia,‡[a] Wenjuan Hu,‡[a] Yuanyuan Zhang,[a] Chao Teng,[a] Zupeng Chen [ID] *[b] and Jian Liu [ID] *[a]

The development of a metal-free photoelectrode film is of great significance. Herein, graphitic carbon nitride (g-C$_3$N$_4$) nanosheets with a concentration of up to 36 mg mL^{-1} were first obtained on a large scale using a wet ball-milling method. The obtained g-C$_3$N$_4$ nanosheets exhibit 6- and 8-times higher activity in terms of photocatalytic H$_2$ evolution and nicotinamide adenine dinucleotide (NADH) regeneration than bulk g-C$_3$N$_4$, respectively. Furthermore, a uniform g-C$_3$N$_4$ film electrode was fabricated *via* the interfacial self-assembly of nanosheets at the air/water interface, which can be transferred onto various substrates. By coupling with graphene nanosheets, a g-C$_3$N$_4$/graphene hybrid film electrode was assembled at the interface, showing improved photoelectrochemical coenzyme NADH regeneration efficiency. The photoelectrochemical system uses water as the electron donor, which avoids the drawback of using additional sacrificial agents. This work presents a novel and facile method to prepare high-quality g-C$_3$N$_4$ hybrid films, and also provides a sustainable route for renewable energy conversion and biocatalytic applications.

Introduction

In recent years, metal-free graphitic carbon nitride (abbreviated as g-C$_3$N$_4$) has attracted enormous interest due to its excellent physicochemical, optical, and chemical properties, extending its applications beyond conventional (photo)catalysis to sensing, solar cells, ion transport and other energy-related applications.[1–6] In addition to the conventional morphology modulation (*e.g.*, nanospheres, monoliths, or nanorods) of nanoparticle samples, g-C$_3$N$_4$ thin films or membranes have emerged as appealing platforms for applications in photoelectrochemical reactions, gas separation, or energy devices.[7–10] Converting solar energy to chemical energy using a photoelectrochemical cell is one of the most promising approaches to meet future energy demands.[11–13] However, the exploitation of g-C$_3$N$_4$ in photoelectrochemical cells has been

limited by the difficulty in coating a layer of high-quality, homogenous g-C$_3$N$_4$ film onto a conductive substrate.[14,15]

Inspired by conventional semiconductor photocatalysts, previous studies have used tedious two-step methods (*e.g.*, spin-coating, electrophoretic deposition) to prepare g-C$_3$N$_4$ film photoelectrodes.[16,17] However, the poor dispersion of g-C$_3$N$_4$ materials in common solvents means that they form poor quality thin films that are inhomogeneous and can be easily detached from electrodes.[18] Since 2015, more and more researchers have attempted to synthesize g-C$_3$N$_4$ film directly from the *in situ* thermal condensation of N-rich precursors onto various substrates, which avoids the poor interfacial engineering problem that usually occurs in conventional two-step deposition methods.[19,20] The thickness of the g-C$_3$N$_4$ film can be controlled using different amounts of precursors and thermal treatment times. However, this method usually requires the use of high-temperature-resistant substrates, excluding the possibility of direct deposition onto a flexible substrate. Therefore, it is still highly desirable to develop a novel strategy to prepare a high-quality g-C$_3$N$_4$ film under mild conditions.

A gas/liquid interface is an ideal platform for assisting the formation of a uniform thin film at the interface *via* the self-assembly of two-dimensional nanosheets, delicately avoiding the aggregation of nanosheets that occurs during calcination or drying processes.[21,22] Herein, we report a versatile wetting-

[a]*College of Materials Science and Engineering, Qingdao University of Science and Technology, Qingdao, 266042, China. E-mail: liujian@qust.edu.cn*
[b]*Institute for Chemical and Bioengineering, Department of Chemistry and Applied Biosciences, ETH Zürich, Zürich, Switzerland. E-mail: zupeng.chen@chem.ethz.ch*

2434 | *Inorg. Chem. Front.*, 2020, **7**, 2434–2442

This journal is © the Partner Organisations 2020

induced transferring strategy at the air/water interface to fabricate a uniform large-area ultrathin g-C$_3$N$_4$ film on arbitrary substrates. Bulk g-C$_3$N$_4$ (BCN) is directly exfoliated into layered nanosheets *via* a modified wet ball milling process, producing a highly stable g-C$_3$N$_4$ nanosheet (CNS) dispersion with a concentration of up to 36 mg mL^{-1}. Due to the facile procedures of the interfacial self-assembly, the film thickness can be easily controlled by varying the transferring times. Conductive graphene nanosheets were coupled with CNS during the interface assembly process to enhance the conductivity of the film electrode and improve the electron–hole separation efficiency. The resulting CNS–graphene (CNS–Gr) hybrid film doubled the photoelectrochemical cofactor NADH regeneration yield in the presence of an electron and proton mediator. This work opens up a new route for the facile preparation of a high-quality g-C$_3$N$_4$ hybrid film with enhanced conductivity and improved electron–hole pair separation efficiency, which render photoelectrochemical NADH regeneration possible using water as an electron donor.[23]

Experimental

Materials

Dicyandiamide, NaH$_2$PO$_4$, Na$_2$HPO$_4$ and triethanolamine (TEOA) were received from Energy Chemical (China). β-NAD$^+$ and graphene were purchased from Aladdin (China). The rhodium complex was synthesized as previously reported.[24] All chemicals were used without further purification. Fluorine-doped tin oxide (FTO) glasses were obtained from PV. Tech (China).

Preparation of BCN

Dicyandiamide was heated at 550 °C for 4 h under atmospheric pressure at a ramp rate of 2 °C min^{-1}, and then cooled to room temperature to obtain a yellow powder.

Preparation of CNS

The CNS were prepared by grinding the BCN through a ball mill at high yield. BCN was added to water, followed by grinding with a 1 : 1 mass ratio of 2 mm ZrO$_2$ and 0.2 mm ZrO$_2$ balls. After ball milling for 60 h, a CNS dispersion was acquired. The dispersion was centrifuged at 500 rpm for 30 min to remove unexfoliated g-C$_3$N$_4$. The supernatant was collected followed by freeze-drying to obtain a CNS powder. A certain amount of CNS was dispersed into ethanol to obtain a dispersion with a concentration of 20 mg mL^{-1}.

Self-assembly of CNS film at the air/water interface

Exfoliated CNS (20 mg mL^{-1}) were dispersed in an ethanol solution, and then the mixture was injected at a certain speed into the air/water interface in a container filled with water. The CNS dispersion began to self-assemble into a homogeneous film at the air/water interface. Then, the water surface was completely covered with CNS by increasing the injected amounts of the CNS dispersion. Afterwards, the film was trans-

ferred to an FTO substrate using a lift-up technique. The FTO glasses (1 × 2.5 cm^2) were washed in advance with acetone, isopropanol, ethanol and deionized water in sequence under continuous ultrasonication.

Self-assembly of a CNS–Gr film at the air/water interface

A CNS–Gr suspension was prepared by adding different amounts (0, 0.2, 0.5, or 0.7 mL) of graphene solution (0.5 wt%) into the CNS dispersion (20 mg mL^{-1}, 3 mL). The same interface assembly method was employed to form a uniform CNS–Gr hybrid film at the air/water interface followed by transferring the film onto FTO, which was further annealed at 350 °C for 2 h under an air atmosphere to enhance the contact between the film and substrate. The obtained films were named as CNS, CNS–Gr$_{0.2}$, CNS–Gr$_{0.5}$, and CNS–Gr$_{0.7}$, respectively.

Photocatalytic H$_2$ production test

Photocatalytic H$_2$ production experiments were performed using a photocatalytic activity evaluation system (CEAULIGHT). A 300 W Xenon arc lamp equipped with a UV-cut-off filter ($\lambda \geq 420$ nm) was employed as the light source to trigger the reaction. The reaction was carried out in an aqueous solution (50 mL) consisting of TEOA (5 mL) and CNS or BCN (25 mg). Pt nanoparticles (3 wt%) were deposited on g-C$_3$N$_4$ by *in situ* photodeposition of H$_2$PtCl$_6$.

Photocatalytic NADH production

Photocatalytic NADH regeneration was carried out in a quartz reactor at room temperature under an air atmosphere using a 36 W LED (450 nm) as the light source. The system consisted of a photocatalyst (BCN and CNS, 6 mg), β-NAD$^+$ (1 mmol), triethanolamine (15 wt%), and rhodium complex (0.25 mmol) in Na$_2$HPO$_4$/NaH$_2$PO$_4$ buffer (3 mL, 0.2 M, pH = 7.4). The NADH regeneration was measured using a UV-vis spectrophotometer (UV-3900, Hitachi).

Photoelectrochemical NADH regeneration tests

Photoelectrochemical (PEC) NADH regeneration tests were conducted in a three-electrode configuration, in which CNS/FTO film (or CNS–Gr/FTO film) was used as the working electrode, a Pt wire as the counter electrode and Ag/AgCl as a reference electrode. The PEC NADH regeneration was carried out at room temperature under a N$_2$ atmosphere using a 300 W Xenon arc lamp equipped with a UV-cut-off filter ($\lambda \geq 420$ nm) as the light source. The NADH-regenerating PEC cell was exposed to visible light at an external bias of −0.9 V. The system consisted of β-NAD$^+$ (1 mmol) and a rhodium complex (0.25 mmol) in Na$_2$HPO$_4$/NaH$_2$PO$_4$ buffer (4 mL, 0.2 M, pH = 7.4). The NADH regeneration was measured using a UV-vis spectrophotometer (UV-3900, Hitachi).

Characterization

Optical transmittance measurements were taken using a UV-vis spectrophotometer (UV-3900, Hitachi). X-ray diffraction (XRD) patterns were measured with Cu Kα radiation in the

This journal is © the Partner Organisations 2020

Inorg. Chem. Front., 2020, **7**, 2434–2442 | **2435**

scanning range from 10° to 70°, X-ray photoelectron spectroscopy (XPS) measurements were taken using a Thermos ESCALAB 250XL spectrometer. Transmission electron microscopy (TEM) was carried out on JEOL JEM-2100 Plus microscope. The Fourier-transform infrared (FTIR) spectroscopy measurements were carried out on a Nicolet iz10 Thermo Scientific spectrometer, scanning from 4000 to 500 cm^{-1}. Scanning electron microscope (SEM) images were obtained using a Zeiss Sigma-300 microscope. Nitrogen adsorption/desorption measurements were performed at 77 K on Micromeritics ASAP 2460 apparatus. Zeta potentials were measured using a Malvern Zeta ZS90 zetasizer. Atomic force microscopy (AFM) images were obtained using a Bruker Multimode 8 microscope. The Mott–Schottky plots were obtained using an electrochemical analyzer (Modulab ECS) with Na$_2$SO$_4$ (0.2 M) aqueous solution. The photocurrent of the CNS/FTO film and electrochemical impedance spectra (EIS) were measured using electrochemical analyzer (CHI660E). The tests were carried out in a standard three-electrode system, where CNS/FTO film (or CNS–Gr/FTO film) acted as the working electrode, a Pt wire as the counter electrode and Ag/AgCl as a reference electrode. In an identical three-electrode system, the EIS measurements were carried out in a range from 1 to 100 kHz at an AC amplitude of 100 mV. Na$_2$SO$_4$ (0.2 M) salt solution was used as the electrolyte.

Results and discussion

Morphological and structural properties

By employing BCN as a starting material, the CNS dispersion could be obtained using a modified wet ball milling method. The concentration of CNS reached up to 36 mg mL^{-1}, one of the highest concentrations reported (Table S1†), making the dispersion milky white (Fig. 1a). A diluted CNS dispersion with a concentration of 0.1 mg mL^{-1} showed good stability even after being stored for three months (Fig. 1b). A typical Tyndall effect was observed in the CNS dispersion (Fig. 1c), suggesting the colloidal nature of the dispersion.[25,26]

The structure and properties of BCN and the resulting CNS were comprehensively characterized by SEM, TEM, XPS, XRD, FTIR spectroscopy, and AFM. As shown in Fig. S1,† the BCN sample has a typical irregular morphology, whereas the exfoliated CNS after ball milling treatment shows a thinner lamellar structure compared with its bulk counterpart, which is evidenced by the representative TEM image shown in Fig. 1d. As shown in the XRD spectra (Fig. 1e), the diffraction peaks of BCN with high intensity are located at 13.5° and 27.6°, ascribed to the in-plane structural repeating unit of the aromatic systems (100) and the typical graphitic interlayer (002) plane, respectively. In the case of CNS, the intensity of the (002) peak significantly decreases while the peak of (100) almost disappears, indicating the efficient exfoliation of BCN into thin layers.[27] This is also consistent with the SEM and TEM observations. The sheet-like morphology and thickness of g-C$_3$N$_4$ is further confirmed by the AFM analysis, showing a
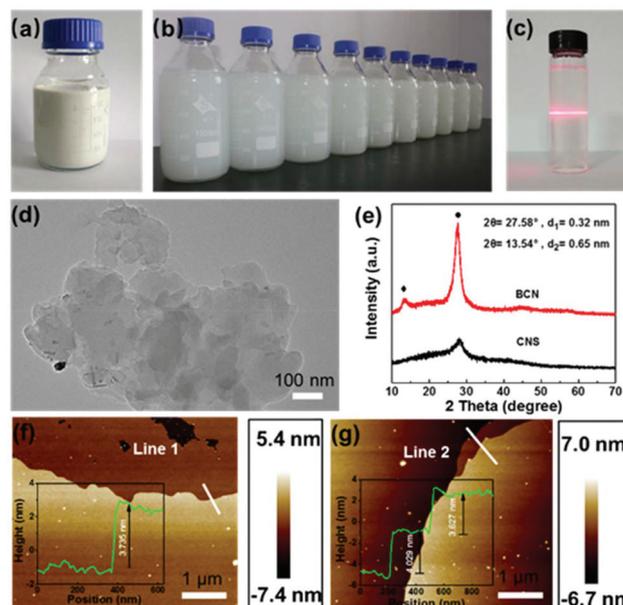

Fig. 1 Digital photo of (a) a concentrated CNS dispersion in water with a concentration of up to 36 mg mL^{-1} after ball milling, and (b) diluted CNS dispersion with a concentration of 0.1 mg mL^{-1}. (c) Tyndall effect of the diluted CNS dispersion. (d) TEM image of the CNS. (e) XRD patterns of BCN and CNS. (f and g) AFM images of CNS.

well-defined nanosheet morphology with a thickness of ~3.85 nm, corresponding to ca. 10 layers (Fig. 1f–g).[28] The above results reveal that the CNS was successfully prepared using a ball milling assisted exfoliation process.

The CNS shows a similar FTIR spectrum to that of BCN, indicating that its structure was preserved after the exfoliation process (Fig. 2a). More specifically, the peak at 810 cm^{-1} can be assigned to the characteristic absorption peak of triazine units in carbon nitride. The peaks ranging from 1170 to 1630 cm^{-1} can be ascribed to the stretching vibrations of CN hetero-

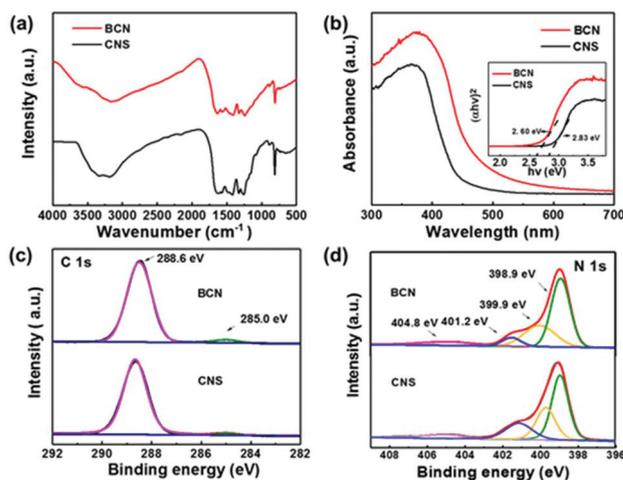**Fig. 2** (a) FTIR, (b) UV-vis absorption spectra, and (c and d) C 1s and N 1s XPS spectra of BCN and CNS.

2436 | *Inorg. Chem. Front.*, 2020, **7**, 2434–2442

This journal is © the Partner Organisations 2020

cycles. The broad band between 2900 and 3600 cm^{-1} can be attributed to N–H stretching vibrations.[29,30] Fig. 2b shows that the optical absorption edge of the CNS blue-shifts by 33 nm with a tail up to 439 nm, compared to that of the BCN (472 nm). The bandgap of the CNS was determined to be *ca.* 2.83 eV according to the Taut plot (($\alpha h\nu$)^2 *versus* $h\nu$), which is greater that the value for BCN (2.60 eV) (Fig. 2b, inset).[30]

Furthermore, the surface chemical compositions and bonding states of BCN and CNS were analyzed by XPS. The survey spectra (Fig. S2†) show the dominant presence of C, N, and O elements both in the bulk and nanosheet forms.[29] The O 1s peak at ~529.7 eV for the g-C$_3$N$_4$ samples can be ascribed to adsorbed water.[31] Both samples show two peaks in the high-resolution C 1s XPS spectra (Fig. 2c): the one located at 285.0 eV can be assigned to C–C in the potential surface impurities of the sp^2 carbon or pseudohalogenic cyano groups (C–C≡N), and the other one situated at 288.6 eV originates from the sp^2 hybridized carbon of tri-*s*-triazine rings (N=C–N$_2$).[31] Meanwhile, the high-resolution N 1s XPS spectra in Fig. 2d can be deconvolved into three main peaks at 398.9, 399.9, and 401.2 eV, which can be attributed to sp^2-hybridized N (C=N–C), tertiary nitrogen (N–(C)$_3$) groups and H-containing amino functional groups (C–NH–C and C–NH$_2$), respectively. Another minor peak at 404.8 eV arises as a result of π-excitations (π → π* transition).[31]

The surface charges of the samples were revealed by Zeta potential analysis. Fig. S3† shows that the Zeta potentials of BCN and CNS were determined to be −31.2 and −36.8 mV in water (pH = 7), respectively. The results imply that the CNS surface has a much more negative potential than that of BCN. Additionally, the N$_2$ adsorption–desorption isotherms show that the Brunauer–Emmett–Teller (BET) specific surface area increases from 6.5 to 34.6 m^2 g^{-1} upon exfoliating BCN into CNS (Fig. S4†).

Photocatalytic behavior of H$_2$ evolution and NADH regeneration

The photocatalytic activities of BCN and CNS were first evaluated by photocatalytic H$_2$ generation under visible light irradiation using TEOA as a hole sacrificial agent (see the schematic illustration in Fig. S5a†).[32,33] Both CNS and BCN can absorb visible light to generate electron–hole pairs. Then, the photogenerated electrons transfer to Pt cocatalysts for reduction of H$_2$O to H$_2$, while the remaining photogenerated holes are consumed by TEOA. Fig. S5b† shows that the CNS exhibit efficient photocatalytic performance towards H$_2$ evolution, which is ~6 times higher than that of the BCN. Moreover, the stability towards the photocatalytic H$_2$ evolution of CNS was demonstrated by three sequential cycling tests that were carried out under the same conditions, which showed no obvious variation in the H$_2$ generation rate. Furthermore, the CNS were employed for cofactor (NAD(P)$^+$/ NAD(P)H) regeneration, which is an important process for sustainable enzymatic synthesis.[34–36] Compared with the conventional electrochemical or enzymatic regeneration, the photocatalytic regeneration method is promising, using light

as the only energy input. The CNS photocatalyst harvests incident visible light with an electronic transition between its HOMO and LUMO orbitals, then transfers the photogenerated electrons to reduce the rhodium complex **M** (**M** = [Cp*Rh(bpy)H$_2$O]$^{2+}$; Cp* = pentamethylcyclopentadienyl, bpy = 2,2′-bipyridine) to **M$_1$**, which further accepts a proton from water. The resulting electron mediator **M$_2$** selectively regenerates NADH by transferring two electrons and one proton to NAD$^+$. The photogenerated holes remaining in the HOMO orbital of CNS are captured by TEOA (Fig. 3a).[37] As a result, CNS exhibits excellent photocatalytic activity for NADH regeneration, reaching 80% yield in 10 minutes, which is much higher than that of the BCN (*ca.* 10%) (Fig. 3b and Fig. S6†). The higher photocatalytic activity of the CNS over that of BCN is as a result of the following merits. First, the CNS have a higher surface area, providing more surface active sites for the photocatalytic reactions and facilitating the surface accessibility of the reactants.[38,39] Second, the reduced thickness in the nanosheets significantly shortens the migration distance of the photogenerated charges from the bulk to the surface, thus enhancing the possibility of them participating in surface redox reactions.[40]

However, the use of TEOA as an electron donor may result in the accumulation of the oxidized state of TEOA$^+$ in the photochemical reaction system, which will deactivate the enzymes and also lead to their separation from the enzymatic reaction products.[41] Therefore, it is desirable to develop a system that is able to achieve visible light driven cofactor regeneration using water as the electron donor. In this regard, the development of the CNS film photoelectrode for PEC is promising and imperative as it can transfer the photogenerated electrons to NAD$^+$ *via* an external wire.[42]

Interfacial Self-assembly of CNS and CNS–Gr hybrid films

The novel interfacial self-assembly procedure of the CNS is illustrated in Scheme 1. The CNS dispersion from wet ball milling was freeze-dried and re-dispersed in ethanol. The nanosheets were self-assembled at the air/water interface *via* slow injection of the nanosheet dispersion into water, a process induced by the Marangoni effect.[43,44] Specifically, the CNS dispersion spreads out at the air/water interface and eventually covers the surface of the container due to the surface free energy gradient between water and ethanol.[45] Finally, by carefully plunging the FTO substrate into water, the CNS film can be transferred from the interface to the conductive FTO
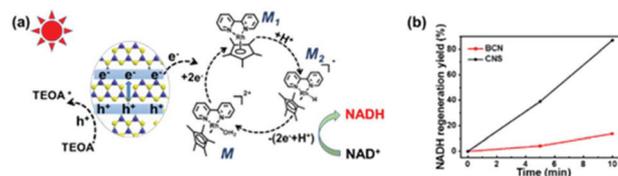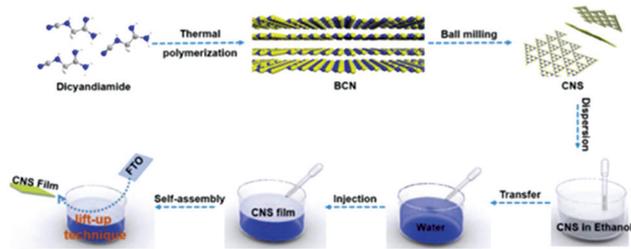

Fig. 3 (a) Illustration of the photocatalytic mechanism of CNS for NADH regeneration, and (b) the NADH regeneration efficiency of BCN and CNS.

This journal is © the Partner Organisations 2020

*Inorg. Chem. Front.,* 2020, **7**, 2434–2442 | **2437**

Scheme 1 Schematic illustration of the self-assembly strategy for CNS film preparation at the water/air interface.

(the film formation process *via* interfacial self-assembly can be seen in Movie S1†). Time-lapse images of the CNS self-assembly process at the air/water interface are shown in Fig. 4a. As a result, a homogeneous and continuous CNS film was successfully transferred from the air/water interface onto the FTO substrate (Fig. 4b–d), exhibiting stacks of laminated nanosheets (Fig. S7a†).

The film thickness can be easily controlled by varying the concentration of the dispersion and the transferring times. For example, the thickness of the CNS film increased from 1.2 to 6.2 μm when increasing the transferred layers from 1 to 3 (Fig. S7b–d,† the resulting samples are coded as CNS-*x*-film, where *x* denotes the number of transferred layers). An integrated CNS–Gr hybrid film electrode was also successfully fabricated *via* the same interface assembly method using a pre-mixed CNS and graphene dispersion (Fig. 4e). The corres-
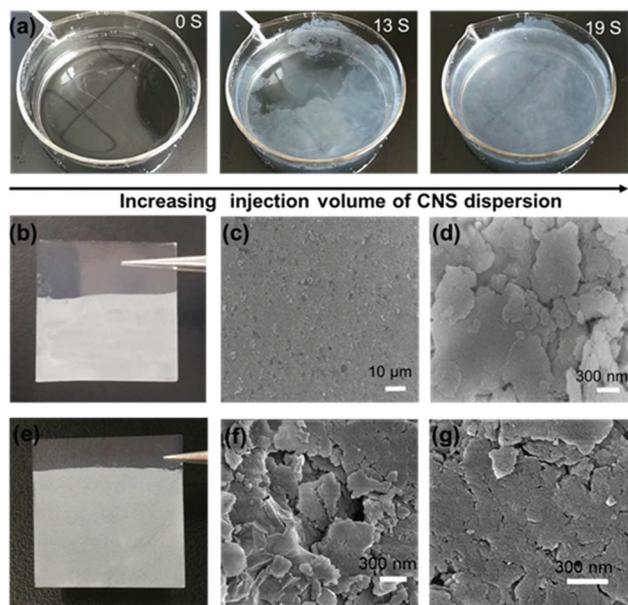
Fig. 4 (a) Time-lapse images of the CNS film self-assembly process at the water/air interface upon the injection of an increasing volume of the CNS dispersion, (b) optical photograph of the CNS film, and SEM images of the CNS film at (c) low magnification, and (d) high magnification, (e) optical photograph of the CNS–Gr$_{0.7}$ film, and (f and g) SEM images of the CNS–Gr$_{0.7}$ film.

ponding SEM images in Fig. 4f–g clearly reveal the close contact between graphene and the CNS, which benefits the transfer of photogenerated electrons. To show the general applicability of the film fabrication method, a CNS–Gr dispersion was transferred onto various substrates such as FTO, a glass slide, frosted glass, flexible substrate, and titanium plate, demonstrating the versatility of the unique film fabrication method (Fig. S8†).

The optical properties of the CNS film with different transferred layers are shown in Fig. S9a,† showing the decreased transmittance upon increasing the thickness. The transient photocurrent density of as-prepared CNS films was investigated under chopped light illumination (Fig. S9b†).[31,46] Although a thicker film increases the light absorbance, the low conductivity of the CNS leads to greater resistance. Therefore, the optimized CNS-2-film exhibited the highest photocurrent density among the three samples due to the trade-off between the light absorbance, penetration, and conductivity. The charge separation and transfer efficiencies of the samples were further characterized using EIS measurements. Nyquist plots of the CNS films under visible light irradiation are shown in Fig. S9c.† The CNS-1 film has the smallest arc radius among the three samples, which indicates its higher charge transfer efficiency. Upon increasing the film thickness, the arc radius of the samples increased owing to the greater resistance. The flat-band potential of the samples was investigated using electrochemical Mott–Schottky (M–S) plots (Fig. S9d†).[31,46] The positive slope of the linear M–S plots reveals the n-type semiconductor characteristics of the CNS film. The flat-band potential of the CNS films was measured to be −1.23 V *versus* Ag/AgCl, which is thermodynamically favorable for the photocatalytic reduction of water and NAD$^+$.[47,48]

Furthermore, the CNS–Gr$_{0.7}$ hybrid film shows a smaller semicircle arc than that of the CNS electrode (Fig. 5a), which indicates that graphene reduces the charge transfer resistance, beneficial to the separation of electron–holes from photoexcited CNS–Gr$_{0.7}$. The Nyquist plots were fitted in terms of the equivalent circuit (the inset), in which R_s, R_{ct} and CPE represent the solution resistance, charge transfer resistance across the interface of electrode/electrolyte, and constant phase element for the electrolyte/electrode interface, respectively.[49] The linear-sweep voltammetry (LSV) curves of CNS and CNS–Gr$_{0.7}$ photocathodes were characterized both under dark and light conditions in phosphate buffer (pH = 7.4). As shown in Fig. 5b, CNS–Gr$_{0.7}$ displays an increased cathodic photocurrent in comparison to CNS, suggesting that the hybrid of graphene with CNS promotes charge separation and transfer.[23] In addition, the UV-Vis absorption spectra clearly reveal that the CNS–Gr$_{0.7}$ hybrid film on FTO has an absorption band edge that is red-shifted to a higher wavelength in comparison to that of the CNS film (Fig. 5c).[50] The CNS and CNS–Gr$_{0.7}$ films were further demonstrated to be hydrophilic from their contact angle measurements (Fig. S10†), which ensure their good contact with the aqueous reaction system.[51]
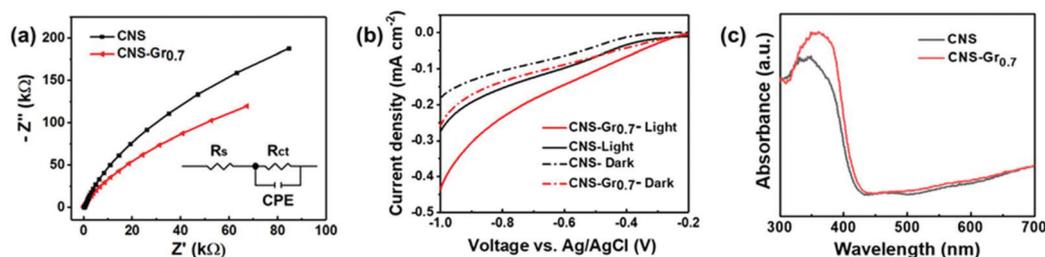
2438 | *Inorg. Chem. Front.*, 2020, **7**, 2434–2442

This journal is © the Partner Organisations 2020

Fig. 5 (a) Nyquist plots and the equivalent circuit (inset), (b) LSV curves in the dark and under light irradiation in phosphate buffer (pH 7.4), and (c) UV-vis absorption spectra of the CNS and CNS–Gr$_{0.7}$ photocathodes.

Photoelectrochemical NADH regeneration of the CNS–Gr hybrid films

Inspired by the process of natural photosynthesis, in which solar energy is converted into chemical energy, a three-electrode PEC system was constructed for efficient coenzyme regeneration, employing the CNS–Gr hybrid film as the photocathode and water as the electron donor (Fig. 6a).[52,53] In this case, the CNS or CNS–Gr film harvests incident visible light, and the resulting photogenerated electrons reduce **M** to **M$_1$**. Then, **M$_1$** accepts a proton from water to generate **M$_2$**. NADH is regenerated when NAD$^+$ takes up two electrons and one proton from **M$_2$**.[42] The sacrificial agent TEOA is not applied in this system, and the photogenerated holes are consumed by the electrons migrating through an external wire to the photocathode. Oxygen is evolved at the Pt anode in the pure water reaction system.[54] The bending of the energy band for CNS under applied bias greatly inhibits the recombination of the photogenerated electron–hole pairs. Cyclic voltammetry was used to study the photoinduced electron-transfer mechanism from the CNS–Gr$_{0.7}$ photocathode to **M** and NAD$^+$.[55,56] As shown in Fig. 6b, the ternary system (CNS–Gr$_{0.7}$ + NAD$^+$ + **M**) exhibits an increased cathodic peak current and a potential shift in comparison with the binary system (CNS–Gr$_{0.7}$ + **M**), indicating that electrons transfer from the CNS–Gr$_{0.7}$ photocathode and **M** to NAD$^+$.[56] Meanwhile, the amount of the hybrid graphene was also investigated, and CNS–Gr$_{0.7}$ was demonstrated to be the optimal sample (Fig. S11†).[53,57] Integration of an excess amount of graphene was found to be detrimental to the photoelectron generation. Under the optimal bias of −0.9 V (vs. Ag/AgCl), the catalytic performance for photoelectrochemical NADH regeneration was studied under visible light, in the presence of **M** as the mediator and water as the electron donor. The concentration of NADH can be measured from its characteristic absorption at λ = 340 nm using a UV-vis spectrophotometer (Fig. S12†). As shown in Fig. 6c, CNS–Gr$_{0.7}$ has double the photoelectrochemical NADH regeneration yield in comparison with CNS. Significantly, the NADH regeneration yield of CNS–Gr$_{0.7}$ was comparable to a previously reported system constructed using a FeOOH/Fe$_2$O$_3$ photoanode and black silicon photocathode with light illumination on both photoelectrodes (Table S2†).[42]

The surface hydroxyl groups of FTO and the terminated amine groups of CNS lead to a strong interaction between the CNS film and FTO substrate.[58] The robustness of the prepared CNS and CNS–Gr$_{0.7}$ films were confirmed by immersing the electrodes in water, which remained intact after 24 h (Fig. S13†). Furthermore, no difference was observed by FTIR (Fig. S14†) and SEM (Fig. S15†) of the used films after the PEC tests, which also suggests the robustness of the prepared films. It is important to note that the reported interfacial self-assembly method can be easily extrapolated to fabricate films of other 2D nanosheet materials (Fig. S16†).
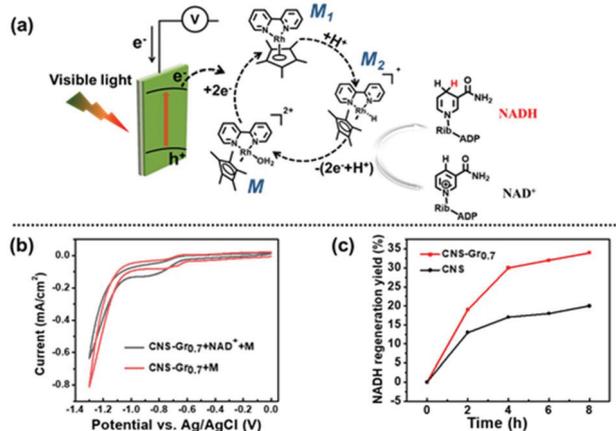

Fig. 6 (a) Illustration of the mechanism of PEC NADH regeneration. (b) Cyclic voltammograms of CNS–Gr$_{0.7}$ in phosphate buffer in the presence of M with or without NAD$^+$. (c) The PEC performance of NADH regeneration of the CNS and CNS–Gr$_{0.7}$ films.

Conclusions

In summary, we successfully synthesized a homogeneous CNS film via interfacial self-assembly of nanosheets at an air/water interface. A CNS dispersion was obtained via a wet ball milling method on a large scale, with a concentration of up to 36 mg mL^{-1}. The as-prepared films could be easily transferred onto versatile substrates with good interfacial contact, which addresses the limitation of the traditional approach of in situ thermal condensation of N-rich precursors on high-temperature-resistant substrates. The high-quality CNS–Gr hybrid films

This journal is © the Partner Organisations 2020

Inorg. Chem. Front., 2020, **7**, 2434–2442 | **2439**

were further assembled on conductive FTO at the interface, enhancing their photoelectrochemical NADH regeneration ability, using $[Cp*Rh(bpy)H_2O]^{2+}$ as the electron and proton mediator and water as the electron donor. The current work sheds light on the fabrication of a high-performance g-C_3N_4 film catalyst and could find more applications in future energy and environmental related devices.[59,60]

Conflicts of interest

There are no conflicts to declare.

Acknowledgements

Notes and references

1 A. Thomas, A. Fischer, F. Goettmann, M. Antonietti, J. O. Müller, R. Schlögl and J. M. Carlsson, ChemInform Abstract: Graphitic Carbon Nitride Materials: Variation of Structure and Morphology and Their Use as Metal-Free Catalysts, *J. Mater. Chem.*, 2008, **18**, 4893–4908.

2 X. Wang, S. Blechert and M. Antonietti, Polymeric Graphitic Carbon Nitride for Heterogeneous Photocatalysis, *ACS Catal.*, 2012, **2**, 1596–1606.

3 J. Liu, H. Wang and M. Antonietti, Graphitic carbon nitride "reloaded": emerging applications beyond (photo)catalysis, *Chem. Soc. Rev.*, 2016, **45**, 2308–2326.

4 Y. Chen, Z. Zhan, J. Wang, Y. Shen, S. Liu and Y. Zhang, Solution-based processing of carbon nitride composite for boosted photocatalytic activities, *Chin. Chem. Lett.*, 2018, **29**, 437–440.

5 X. Wang, K. Maeda, A. Thomas, K. Takanabe, G. Xin, J. M. Carlsson, K. Domen and M. Antonietti, A metal-free polymeric photocatalyst for hydrogen production from water under visible light, *Nat. Mater.*, 2009, **8**, 76–80.

6 X.-H. Li, X. Wang and M. Antonietti, Solvent-Free and Metal-Free Oxidation of Toluene Using O_2 and g-C_3N_4 with Nanopores: Nanostructure Boosts the Catalytic Selectivity, *ACS Catal.*, 2012, **2**, 2082–2086.

7 Y. Wang, L. Li, Y. Wei, J. Xue, H. Chen, L. Ding, J. Caro and H. Wang, Water Transport with Ultralow Friction through Partially Exfoliated g-C_3N_4 Nanosheet Membranes with Self-Supporting Spacers, *Angew. Chem., Int. Ed.*, 2017, **129**, 8974–8980.

8 J. Duan, S. Chen, M. Jaroniec and S. Z. Qiao, Porous C_3N_4 nanolayers@N-graphene films as catalyst electrodes for highly efficient hydrogen evolution, *ACS Nano*, 2015, **9**, 931–940.

9 Z. Chen, H. Wang, J. Xu and J. Liu, Surface Engineering of Carbon Nitride Electrode by Molecular Cobalt Species and Their Photoelectrochemical Application, *Chem. – Asian J.*, 2018, **13**, 1539–1543.

10 J. Liu, H. Wang, Z. P. Chen, H. Moehwald, S. Fiechter, R. van de Krol, L. Wen, L. Jiang and M. Antonietti, Microcontact-Printing-Assisted Access of Graphitic Carbon Nitride Films with Favorable Textures toward Photoelectrochemical Application, *Adv. Mater.*, 2015, **27**, 712–718.

11 Y. Wang, W. Tian, L. Chen, F. Cao and L. Li, Three-Dimensional WO_3 Nanoplate/Bi_2S_3 Nanorod Heterojunction as a Highly Efficient Photoanode for Improved Photoelectrochemical Water Splitting, *ACS Appl. Mater. Interfaces*, 2017, **9**, 40235–40243.

12 Y. Wang, W. Tian, C. Chen, W. Xu and L. Li, Tungsten Trioxide Nanostructures for Photoelectrochemical Water Splitting: Material Engineering and Charge Carrier Dynamic Manipulation, *Adv. Funct. Mater.*, 2019, **29**, 1809036.

13 C. Chen, W. Tian, W. Xu, F. Cao and L. Li, Structure and Band Alignment Engineering of CdS/TiO_2/Bi_2WO_6 Trilayer Nanoflake Array for Efficient Photoelectrochemical Water Splitting, *ChemElectroChem*, 2019, **6**, 5248–5254.

14 L. Ye, D. Wang and S. Chen, Fabrication and Enhanced Photoelectrochemical Performance of MoS_2/S-Doped g-C_3N_4 Heterojunction Film, *ACS Appl. Mater. Interfaces*, 2016, **8**, 5280–5289.

15 C. Xiang, Q. Liu, Q. Wu, P. Du, J. Zhu, S. Dai and S. Yang, Incorporating Graphitic Carbon Nitride (g-C_3N_4) Quantum Dots into Bulk-Heterojunction Polymer Solar Cells Leads to Efficiency Enhancement, *Adv. Funct. Mater.*, 2016, **26**, 1719–1728.

16 S. Li, G. Dong, R. Hailili, L. Yang, Y. Li, F. Wang, Y. Zeng and C. Wang, Effective photocatalytic H_2O_2 production under visible light irradiation at g-C_3N_4 modulated by carbon vacancies, *Appl. Catal., B*, 2016, **190**, 26–35.

17 N. Sagara, S. Kamimura, T. Tsubota and T. Ohno, Photoelectrochemical CO_2 reduction by a p-type boron-doped g–C_3N_4 electrode under visible light, *Appl. Catal., B*, 2016, **192**, 193–198.

18 Y. Zhang, T. Mori, J. Ye and M. Antonietti, Phosphorus-Doped Carbon Nitride Solid: Enhanced Electrical Conductivity and Photocurrent Generation, *J. Am. Chem. Soc.*, 2010, **132**, 6294–6295.

19 J. Bian, J. Li, S. Kalytchuk, Y. Wang, Q. Li, T. C. Lau, T. A. Niehaus, A. L. Rogach and R.-Q. Zhang, Efficient emission facilitated by multiple energy level transitions in uniform graphitic carbon nitride films deposited by thermal vapor condensation, *ChemPhysChem*, 2015, **16**, 954–959.

20 F. Jia, Y. Zhang, W. Hu, M. Lv, C. Jia and J. Liu, *In situ* Construction of Superhydrophilic g-C_3N_4 Film by Vapor-Assisted Confined Deposition for Photocatalysis, *Front. Mater.*, 2019, **6**, 52.

2440 | *Inorg. Chem. Front.*, 2020, **7**, 2434–2442

This journal is © the Partner Organisations 2020

21 J. Wang, C. Teng, Y. Jiang, Y. Zhu and L. Jiang, Wetting-Induced Climbing for Transferring Interfacially Assembled Large-Area Ultrathin Pristine Graphene Film, *Adv. Mater.*, 2019, **31**, 1806742.

22 C. Teng, Y. Lin, Y. Tan, J. Liu and L. Wang, Facile Assembly of a Large-Area BNNSs Film for Oxidation/Corrosion-Resistant Coatings, *Adv. Mater. Interfaces*, 2018, **5**, 1800750.

23 E. J. Son, S. H. Lee, S. K. Kuk, M. Pesic, D. S. Choi, J. W. Ko, K. Kim, F. Hollmann and C. B. Park, Carbon Nanotube-Graphitic Carbon Nitride Hybrid Films for Flavoenzyme-Catalyzed Photoelectrochemical Cells, *Adv. Funct. Mater.*, 2018, **28**, 1705232.

24 J. Liu and M. Antonietti, Bio-inspired NADH regeneration by carbon nitride photocatalysis using diatom templates, *Energy Environ. Sci.*, 2013, **6**, 1486–1493.

25 L. Dan, M. B. Müller, G. Scott, R. B. Kaner and G. G. Wallace, Processable aqueous dispersions of graphene nanosheets, *Nat. Nanotechnol.*, 2008, **3**, 101–105.

26 C. Teng, D. Xie, J. Wang, Z. Yang, G. Ren and Y. Zhu, Ultrahigh Conductive Graphene Paper Based on Ball-Milling Exfoliated Graphene, *Adv. Funct. Mater.*, 2017, **27**, 1700240.

27 Y. Li, R. Jin, Y. Xing, J. Li, S. Song, X. Liu, M. Li and R. Jin, Macroscopic Foam-Like Holey Ultrathin g-C$_3$N$_4$ Nanosheets for Drastic Improvement of Visible-Light Photocatalytic Activity, *Adv. Energy Mater.*, 2016, **6**, 1601273.

28 Y. Yu, Y. Wei, X. Wang, L. Pei and K. Ding, Surface Engineering for Extremely Enhanced Charge Separation and Photocatalytic Hydrogen Evolution on g-C$_3$N$_4$, *Adv. Mater.*, 2018, **30**, 1705060.

29 Z. Jiang, X. Zhang, J. Wang, L. Chen, H. S. Chen and P. Yang, Ultrastable g-C$_3$N$_4$ assemblies with high quantum yield and reversible photoluminescence, *Chem. Commun.*, 2018, **54**, 13519–13522.

30 Z. Chen, T.-T. Fan, X. Yu, Q.-L. Wu, Q.-H. Zhu, L.-Z. Zhang, J.-H. Li, W.-P. Fang and X.-D. Yi, Gradual carbon doping of graphitic carbon nitride towards metal-free visible light photocatalytic hydrogen evolution, *J. Mater. Chem. A*, 2018, **6**, 15310–15319.

31 P. Xia, M. Antonietti, B. Zhu, T. Heil, J. Yu and S. Cao, Designing Defective Crystalline Carbon Nitride to Enable Selective CO$_2$ Photoreduction in the Gas Phase, *Adv. Funct. Mater.*, 2019, **29**, 1900093.

32 J. Liu, J. Huang, H. Zhou and M. Antonietti, Uniform graphitic carbon nitride nanorod for efficient photocatalytic hydrogen evolution and sustained photoenzymatic catalysis, *ACS Appl. Mater. Interfaces*, 2014, **6**, 8434–8440.

33 J. Huang, M. Antonietti and J. Liu, Bio-inspired carbon nitride mesoporous spheres for artificial photosynthesis: Photocatalytic cofactor regeneration for sustainable enzymatic synthesis, *J. Mater. Chem. A*, 2014, **2**, 7686–7693.

34 Q. Pan, H. Liu, Y. Zhao, S. Chen, B. Xue, X. Kan, X. Huang, J. Liu and Z. Li, Preparation of N-Graphdiyne Nanosheets at Liquid/Liquid Interface for Photocatalytic NADH Regeneration, *ACS Appl. Mater. Interfaces*, 2019, **11**, 2740–2744.

35 X. Wang, T. Saba, H. H. P. Yiu, R. F. Howe, J. A. Anderson and J. Shi, Cofactor NAD(P)H Regeneration Inspired by Heterogeneous Pathways, *Chem*, 2017, **2**, 621–654.

36 J. Liu, R. Cazelles, Z. P. Chen, H. Zhou, A. Galarneau and M. Antonietti, The bioinspired construction of an ordered carbon nitride array for photocatalytic mediated enzymatic reduction, *Phys. Chem. Chem. Phys.*, 2014, **16**, 14699–14705.

37 A. Kumar, R. K. Yadav, N.-J. Park and J.-O. Baeg, Facile One-Pot Two-Step Synthesis of Novel in Situ Selenium-Doped Carbon Nitride Nanosheet Photocatalysts for Highly Enhanced Solar Fuel Production from CO$_2$, *ACS Appl. Nano Mater.*, 2017, **1**, 47–54.

38 J. Zhang, Y. Chen and X. Wang, Two-dimensional covalent carbon nitride nanosheets: synthesis, functionalization, and applications, *Energy Environ. Sci.*, 2015, **8**, 3092–3108.

39 Y. Wang, H. Liu, Q. Pan, C. Wu, W. Hao, J. Xu, R. Chen, J. Liu, Z. Li and Y. Zhao, Construction of Fully Conjugated Covalent Organic Frameworks via Facile Linkage Conversion for Efficient Photoenzymatic Catalysis, *J. Am. Chem. Soc.*, 2020, **142**, 5958–5963.

40 H. Tong, S. Ouyang, Y. Bi, N. Umezawa, M. Oshikiri and J. Ye, Nano-photocatalytic materials: possibilities and challenges, *Adv. Mater.*, 2012, **24**, 229–251.

41 S. H. Lee, J. H. Kim and C. B. Park, Coupling photocatalysis and redox biocatalysis toward biocatalyzed artificial photosynthesis, *Chem. – Eur. J.*, 2013, **19**, 4392–4406.

42 D. H. Nam, G. M. Ryu, S. K. Kuk, D. S. Choi, E. J. Son and C. B. Park, Water oxidation-coupled, photoelectrochemical redox biocatalysis toward mimicking natural photosynthesis, *Appl. Catal., B*, 2016, **198**, 311–317.

43 X. Fanton, A. M. Cazabat and D. Quéré, Thickness and Shape of Films Driven by a Marangoni Flow, *Langmuir*, 1996, **12**, 5875–5880.

44 L. E. Scriven and C. V. Sternling, The Marangoni Effects, *Nature*, 1960, **187**, 186–188.

45 X. Li, T. Yang, Y. Yao, Z. Jia and H. Zhu, Large-Area Ultrathin Graphene Films by Single-Step Marangoni Self-Assembly for Highly Sensitive Strain Sensing Application, *Adv. Funct. Mater.*, 2016, **26**, 1322–1329.

46 J. Zhang, M. Zhang, L. Lin and X. Wang, Sol Processing of Conjugated Carbon Nitride Powders for Thin-Film Fabrication, *Angew. Chem., Int. Ed.*, 2015, **54**, 6297–6301.

47 S. H. Lee, D. S. Choi, S. K. Kuk and C. B. Park, Photobiocatalysis: Activating Redox Enzymes by Direct or Indirect Transfer of Photoinduced Electrons, *Angew. Chem., Int. Ed.*, 2018, **57**, 7958–7985.

48 S. Yang, Y. Gong, J. Zhang, L. Zhan, L. Ma, Z. Fang, R. Vajtai, X. Wang and P. M. Ajayan, Exfoliated graphitic carbon nitride nanosheets as efficient catalysts for hydrogen evolution under visible light, *Adv. Mater.*, 2013, **25**, 2452–2456.

49 S. Hong, S. Lee, J. Jang and J. Lee, Heterojunction BiVO$_4$/WO$_3$ electrodes for enhanced photoactivity of water oxidation, *Energy Environ. Sci.*, 2011, **4**, 1781–1787.

50 G. Peng, M. Volokh, J. Tzadikov, J. Sun and M. Shalom, Carbon Nitride/Reduced Graphene Oxide Film with

This journal is © the Partner Organisations 2020

Inorg. Chem. Front., 2020, **7**, 2434–2442 | **2441**

Enhanced Electron Diffusion Length: An Efficient Photo-Electrochemical Cell for Hydrogen Generation, *Adv. Energy Mater.*, 2018, **8**, 1800566.

51 X. Shan, J. Liu, H. Mu, Y. Xiao, B. Mei, W. Liu, G. Lin, Z. Jiang, L. Wen and L. Jiang, An Engineered Superhydrophilic/Superaerophobic Electrocatalyst Composed of the Supported CoMoSx Chalcogel for Overall Water Splitting, *Angew. Chem., Int. Ed.*, 2020, **59**, 1659–1665.

52 J. Kim and C. B. Park, Shedding light on biocatalysis: photoelectrochemical platforms for solar-driven biotransformation, *Curr. Opin. Chem. Biol.*, 2019, **49**, 122–129.

53 S. K. Kuk, R. K. Singh, D. H. Nam, R. Singh, J.-K. Lee and C. B. Park, Photoelectrochemical Reduction of Carbon Dioxide to Methanol through a Highly Efficient Enzyme Cascade, *Angew. Chem., Int. Ed.*, 2017, **56**, 3827–3832.

54 T. Inoue and T. Yamase, Photoelectrochemical cell using sic for water splitting, *Chem. Lett.*, 1985, **14**, 869–872.

55 R. Cazelles, J. Liu and M. Antonietti, Hybrid C_3N_4/Fluorine-Doped Tin Oxide Electrode Transfers Hydride for 1,4-NADH Cofactor Regeneration, *ChemElectroChem*, 2015, **2**, 333–337.

56 R. K. Yadav, G. H. Oh, N.-J. Park, A. Kumar, K.-J. Kong and J.-O. Baeg, Highly Selective Solar-Driven Methanol from CO_2 by a Photocatalyst/Biocatalyst Integrated System, *J. Am. Chem. Soc.*, 2014, **136**, 16728–16731.

57 Y. W. Lee, P. Boonmongkolras, E. J. Son, J. Kim, S. H. Lee, S. K. Kuk, J. W. Ko, B. Shin and C. B. Park, Unbiased biocatalytic solar-to-chemical conversion by FeOOH/BiVO$_4$/perovskite tandem structure, *Nat. Commun.*, 2018, **9**, 4208.

58 G. Peng, L. Xing, J. Barrio, M. Volokh and M. Shalom, A General Synthesis of Porous Carbon Nitride Films with Tunable Surface Area and Photophysical Properties, *Angew. Chem., Int. Ed.*, 2018, **57**, 1186–1192.

59 W. Liu, M. Zhu, J. Liu, X. Li and J. Liu, Flexible asymmetric supercapacitor with high energy density based on optimized MnO_2 cathode and Fe_2O_3 anode, *Chin. Chem. Lett.*, 2019, **30**, 750–756.

60 C. Han, P. Meng, E. Waclawik, C. Zhang, X. Li, H. Yang, M. Antonietti and J. Xu, Palladium/Graphitic Carbon Nitride (g-C_3N_4) Stabilized Emulsion Microreactor as a Store for Hydrogen from Ammonia Borane for Use in Alkene Hydrogenation, *Angew. Chem., Int. Ed.*, 2018, **57**, 14857–14861.

2442 | *Inorg. Chem. Front.*, 2020, **7**, 2434–2442

This journal is © the Partner Organisations 2020